### Title

A High-Energy NASICON-Type Cathode Material for Na-Ion Batteries




### Journal

Advanced Energy Materials, 10(10)

### ISSN

1614-6832



### Authors

Wang, J
Wang, Y
Seo, DH
et al.



### Publication Date

2020-03-01

### DOI

10.1002/aenm.201903968

Peer reviewed

# A High-energy NASICON-type Cathode Material for Na-ion Batteries

*Jingyang Wang [a, b], Yan Wang [c, *], Dong-Hwa Seo [c], Tan Shi [a, b], Shouping Chen [a, b], Yaosen Tian [a, b], Haegyeom Kim [a] and Gerbrand Ceder [a, b, *]*

*corresponding author:
*Dr. Yan Wang (Email: eric.wangyan@samsung.com)*
*Prof. Gerbrand Ceder (Email: gceder@berkeley.edu*)

[a] Materials Sciences Division, Lawrence Berkeley National Laboratory, Berkeley, CA 94720, USA
[b] Department of Materials Science and Engineering, University of California, Berkeley, CA 94720, USA
[c] Advanced Material Lab, Samsung Research America, MA 01803, USA.

## Abstract

Over the last decade, Na-ion batteries have been extensively studied as low-cost alternatives to Li-ion batteries for large-scale grid storage applications; however, the development of high-energy positive electrodes remains a major challenge. Materials with a polyanionic framework, such as NASICON-structured cathodes with formula Na$xM_2(PO_4)_3$, have attracted considerable attention because of their stable three-dimensional crystal structure, and high operating potential. Herein, we report a novel NASICON-type compound, $Na_4MnCr(PO_4)_3$, as a promising cathode material for Na-ion batteries that delivers a high specific capacity of 130 mAh $g^{-1}$ during discharge utilizing high-voltage $Mn^{2+/3+}$ (3.5 V), $Mn^{3+/4+}$ (4.0 V), and $Cr^{3+/4+}$ (4.35 V) transition metal redox. In addition, $Na_4MnCr(PO_4)_3$ exhibits high rate capability (97 mAh $g^{-1}$ at 5C) and excellent all-temperature performance (negligible capacity loss at −10 °C and 50 °C). *In situ* X-ray diffraction and synchrotron X-ray

diffraction analyses reveal reversible structural evolution for both charge and discharge.

## Introduction

The abundance and widespread distribution of sodium make Na-ion batteries a significantly less expensive alternative to Li-ion batteries, which is particularly attractive for large-scale grid storage applications.[1] Nevertheless, to make Na-ion batteries competitive, the development of high-energy cathode materials is crucial.[2] Extensive efforts have thus been devoted to the investigation of Na-ion cathode materials, especially sodium layered oxides and polyanionic compounds.[3] Despite the high specific capacity of layered compounds,[4] they often lack structural stability in the highly charged state and require a low discharge cutoff voltage to achieve enough capacity.[5] In contrast, polyanionic compounds usually have a three-dimensional (3D) robust framework that provides better cycling stability and a flatter voltage profile compared with those of layered oxides. In addition, owing to the inductive effect of the polyanion group (*e.g.,* $(PO_4)^{3-}$, $(P_2O_7)^{4-}$, $(SO_4)^{2-}$), a higher operating voltage can be achieved,[6] making these compounds interesting candidates for stable, high-energy-density cathode materials for Na-ion batteries.

The most studied polyanionic Na-ion cathode materials are the vanadium-containing phosphate $Na_3V_2(PO_4)_3$ (NVP)[7, 8] and the fluorophosphate

$Na_3V_2(PO_4)_2F_3$ (NVPF).[9] NVPF delivers a capacity of 128 mAh $g^{-1}$ (two electrons per formula unit) at 3.9 V, with specific energy reaching 500 Wh $kg^{-1}$. Moreover, the electrochemical properties of NVPF can be tuned by substituting F anions by O, forming the complete solid solution $Na_3V_2(PO_4)_2F_{3-2y}O_{2y}$.[10] For example, Bianichi *et al.* showed that at the low-voltage end, an additional Na can be inserted in $Na_3V_2(PO_4)_2O_2F$ to produce $Na_4V_2(PO_4)_2O_2F$ upon discharge, which enables three-electron cycling between $Na_4V_2(PO_4)_2O_2F$ and $NaV_2(PO_4)_2O_2F$.[11] However, the extraction of the third Na from $NaV_2(PO_4)_2F_3$ to $V_2(PO_4)_2F_3$ has not yet been demonstrated to be practical because of the high Na extraction potential (predicted to be ≈4.9 V), which is beyond the stability window of organic Na-ion electrolytes.[12] Cation substitution has been considered in an effort to lower this high Na extraction voltage; however, only few metal cations, such as Al, can substitute for V in the NVPF structure, with their solubility limited to 0.2.[11, 13]

NVP has a Na superionic conductor (NASICON)-type structure. Na-ion cathode materials with the NASICON structure tend to have high multi-electron capacity, a stable framework, and fast Na diffusion.[14] NVP has the general chemical formula $Na_xMM'(PO_4)_3$, where *M* and *M'* represent transition metals and *x* can vary between 1 and 4.[15, 16] The 3D host framework of NVP is built up by interlinking $[MO_6]$ octahedra and $[PO_4]$ tetrahedra via corner-shared oxygen; the strong covalent bonding results in good thermal stability and long cycle life. This open framework also provides 3D open channels for fast

Na-ion diffusion, yielding excellent rate performance.[17, 18] Numerous NASICON-type compounds with different metal cation combinations ($V_2$, MnV, MnTi, MnZr, VCr, VGa, NiV, FeV, *etc.*) have been synthesized and studied,[15, 16, 19-24] giving rise to a much more diverse chemical space and tunable electrochemical properties in contrast to NVPF. Though NASICON-type compounds have a large Na reservoir with potentially up to four extractable Na (*i.e.,* a theoretical capacity of ~220 mAh $g^{-1}$), reversible extraction/insertion of more than 2Na can rarely be achieved. NVP delivers a discharge capacity of 110 mAh $g^{-1}$ with an average voltage of 3.4 V based on the $V^{3+/4+}$ redox. Partially substituting Al, Ga, or Cr for V can slightly increase the energy density by activating the high-voltage $V^{4+/5+}$ redox;[8, 21, 22] nevertheless, the capacity remains limited to a 2Na capacity. Replacing one V with Mn leads to another well-known NASICON-type compound, $Na_4MnV(PO_4)_3$ (NMVP), from which 3Na can be electrochemically extracted when charged to 4.3 V *vs.* Na metal.[25, 26] However, a recent *in situ* X-ray diffraction (XRD) study performed by Chen *et al.* revealed that NMVP undergoes an irreversible structural change after 3Na deintercalation and that only ~2Na can be intercalated back, with poor cycling stability observed for the second and subsequent cycles.[25] Other Mn-based NASICONs such as $Na_3MnZr(PO_4)_3$ (NMZP) and $Na_3MnTi(PO_4)_3$ (NMTP)[19, 27] exhibit stable cycling based on $Mn^{2+/3+}$ and $Mn^{3+/4+}$ redox; however, the theoretical capacities are also limited to 2Na because Zr and Ti are not electrochemically active at a useful cathode potential. Recently, Zhu *et al.* reported that NMTP can be

initially discharged to 1.5 V, uptaking one more Na from the electrolyte/Na metal anode, with 3Na cycling achieved between the $Na_4MnTi(PO_4)_3$ and $NaMnTi(PO_4)_3$ phase; however, the voltage based on $Ti^{3+/4+}$ redox is too low (2.1 V).[28] Therefore, to further increase the energy density of NASICON-type cathodes, the discovery of a new compound is needed to activate 3Na cycling at high voltage.

In this work, we computationally designed and experimentally synthesized a novel NASICON-type compound $Na_4MnCr(PO_4)_3$ (NMCP), achieving for the first time reversible 2.35Na (de)intercalation at the highest average voltage (3.59 V) among NASICON-type cathodes to date. Reversible transition metal redox ($Mn^{2+/3+}$, $Mn^{3+/4+}$, and $Cr^{3+/4+}$) is confirmed by X-ray absorption spectroscopy. Moreover, *in situ* XRD and synchrotron XRD analyses reveal a combined single-phase, two-phase and single-phase reversible Na (de)intercalation mechanism during cycling of this novel NASICON-type compound.

## Results

The feasibility of synthesizing the Mn/Cr-based NMCP was evaluated and compared with that of $Na_xMnM(PO_4)_3$ (M= Ti, Zr) with the same NASICON structure using density functional theory (DFT) calculations. Ground state phase diagram were computed by generating the respective quaternary

convex hulls constrained with all the competing phases present in the Materials Project.[29] The calculated phase stabilities are summarized in Table S1. The Mn/Cr-based NMCP compound has a relatively low energy above the hull (< 25 meV/atom) across the full Na1–Na4 region, suggesting synthetic accessibility and good structural stability upon Na extraction/reinsertion. Figure 1 presents the DFT-calculated voltage profile of $Na_xMnM(PO_4)_3$ (M=Cr, Ti, Zr, x=0, 1, 2, 3, 4) averaged between the discrete Na compositions.[30] The combination of $Mn^{2+/3+}$, $Mn^{/3+/4+}$, and $Cr^{3+/4+}$ redox couples in NMCP is predicted to provide an average voltage close to 4 V and a theoretical capacity of 165 mAh $g^{-1}$, which is the highest capacity among $Na_xMnM(PO_4)_3$ (M=Cr, Ti, Zr) materials.

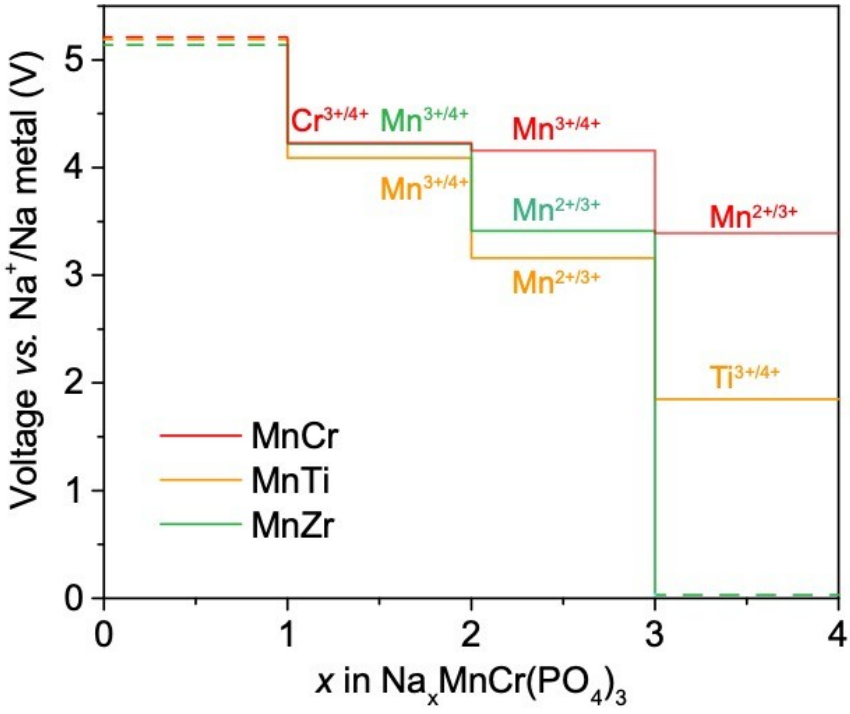


*Figure 1: Calculated voltage profiles for $Na_xMnM(PO_4)_3$ (M = Cr, Ti, Zr; x=0, 1, 2, 3, 4) obtained using DFT calculations. The dashed lines are considered*

*inaccessible voltages according to the phase stability analysis (supplementary information).*

The NMCP compounds were synthesized by mixing the precursors through a sol-gel method followed by pre-heating the product at 400 ℃ and annealing at 650 ℃ in an argon atmosphere (Methods). The synchrotron XRD data for NMCP are presented in Figure 2a with no obvious impurity phases observed. The as-synthesized NMCP has the typical NASICON structure (Figure 2b) with rhombohedral space group *R-3c* and lattice parameters $a = b = 8.9228(5)$ Å, $c = 21.471(1)$ Å as obtained from Rietveld refinement, yielding a volume $V = 1480.4(1)$ Å$^3$ per unit cell. The values of $a$ and $c$ are slightly smaller than those reported for NMVP,[16] consistent with the smaller ionic radius of $Cr^{3+}$ (0.615 Å) relative to that of $V^{3+}$ (0.64 Å). There are two distinct sodium sites in the structure as shown in Figure 2b, the 6b site with six-fold coordination ($Na_1$) and the 18e site with eight-fold coordination ($Na_2$). The Na occupancies obtained from the Rietveld refinement are 1 for $Na_1$ and 0.999 for $Na_2$ (Table S2), which confirms that both Na sites are fully occupied and in good agreement with the nominal composition $Na_4MnCr(PO_4)_3$. Detailed crystallographic data from the Rietveld refinement are provided in Table S2. Figure 2c presents a high-angle annular dark-field (HAADF) scanning transmission electron microscopy (STEM) image of a single NMCP particle. The corresponding energy-dispersive X-ray spectroscopy (EDX) elemental mapping demonstrates a uniform distribution of Na, Mn, and Cr. The size and morphology of the as-synthesized NMCP was characterized using scanning

electron microscopy (SEM), as shown in Figure S1a and b, revealing that the particle size of NMCP is not evenly distributed and ranges from several to tens of micrometers. The large particle size implies that the electrochemical performance of NMCP can possibly be improved by morphology optimization.

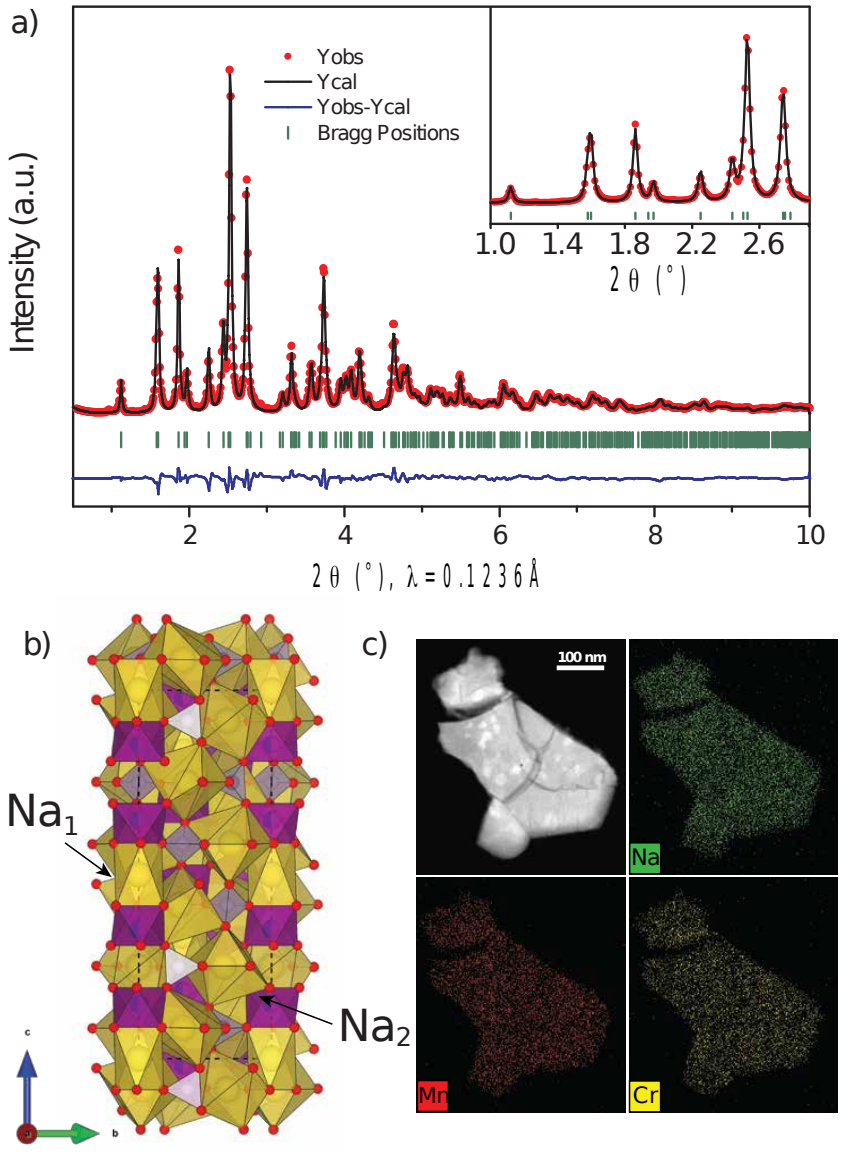


*Figure 2: a) Rietveld refinement of synchrotron XRD data of as-synthesized $Na_4MnCr(PO_4)_3$. b) Structure of $Na_4MnCr(PO_4)_3$ obtained from Rietveld refinement of synchrotron XRD data, with the purple units representing $[(Mn/Cr)O_6]$ octahedra and the light purple $[PO_4]$ tetrahedra and yellow units representing*

*the coordination of Na. c) HAADF image of a NMCP particle and corresponding EDX mapping obtained using STEM.*

The electrochemical performance of NMCP as a positive electrode was tested in a Na half-cell. Figure 3a presents the voltage *vs.* capacity curve of NMCP for the first two cycles between 1.5 and 4.5 V at C/20 (1C = 110 mAh $g^{-1}$). NMCP delivers a large first charge capacity of 141 mAh $g^{-1}$ and discharge capacity of 130 mAh $g^{-1}$, corresponding to 2.6 Na extraction and 2.35 Na reinsertion. Distinct plateaus appear in the voltage profile during charge (discharge) at 3.6 V (3.5 V), 4.2 V (4.1 V), and 4.4 V (4.35 V), as confirmed by the three oxidation and reduction peaks observed in the differential capacity ($dQ\ dV^{-1}$) curve (inset). When further discharged to 1.0 V, an additional low-voltage tail appears, and the overall discharge capacity reaches 157 mAh $g^{-1}$, with a coulombic efficiency of ~100% (Figure 3b). This low-voltage capacity is highly reversible in the subsequent cycles.

The cycling performance of NMCP in different voltage windows is summarized in Figure 3c. When cycled between 1.5 and 4.5 V, the discharge capacity of NMCP fades to 90 mAh $g^{-1}$ (120 mAh $g^{-1}$) after 20 cycles, whereas the coulombic efficiency gradually increases from 91% to 97%. The capacity retention can be improved by decreasing the high-voltage cutoff to 4.35 V (88% retention after 20 cycles), although the initial discharge capacity is reduced to 96 mAh $g^{-1}$. These results indicate that the capacity fading of NMCP may originate from the capacity loss in the high-voltage

region. At this point, we do not know if this capacity loss at high voltage is due to electrolyte failure or an intrinsic degradation of the material.

The Na diffusion kinetics of NMCP was investigated by means of the galvanostatic intermittent titration (GITT) and rate testing. Figure 3d presents the GITT curve for the second cycle. A small overpotential (20–30 mV) is observed during most of the charge and discharge, demonstrating good kinetics for Na diffusion, especially at high voltage when the composition has low Na content (red). A larger overpotential is present in the lower voltage regions, marked by the orange and blue regions in the time *vs.* voltage plot (inset). At the end of discharge, the overpotential for Na insertion is 324 mV, and 200 mV for Na extraction when the charge is started. The rate performance of NMCP was tested in a half-cell cycled between 1.5 and 4.5 V. As shown in Figure 3e, NMCP exhibits excellent rate capability with discharge capacities of 105 and 97 mAh $g^{-1}$ at 2C and 5C, respectively, corresponding to 81% and 75% of the discharge capacity at C/20. Interestingly, the capacity loss at increased rate is mainly associated with the low-voltage region, and the high-voltage plateaus are better maintained upon increasing the current (Figure 3f). This rate test confirms the finding in the GITT experiment that Na diffusion kinetics is very good in the Na deficient phase. Even though the cathode particles are micro-sized, this rate performance is comparable to that of other reported nano-sized NASICONs.[19, 28, 31]

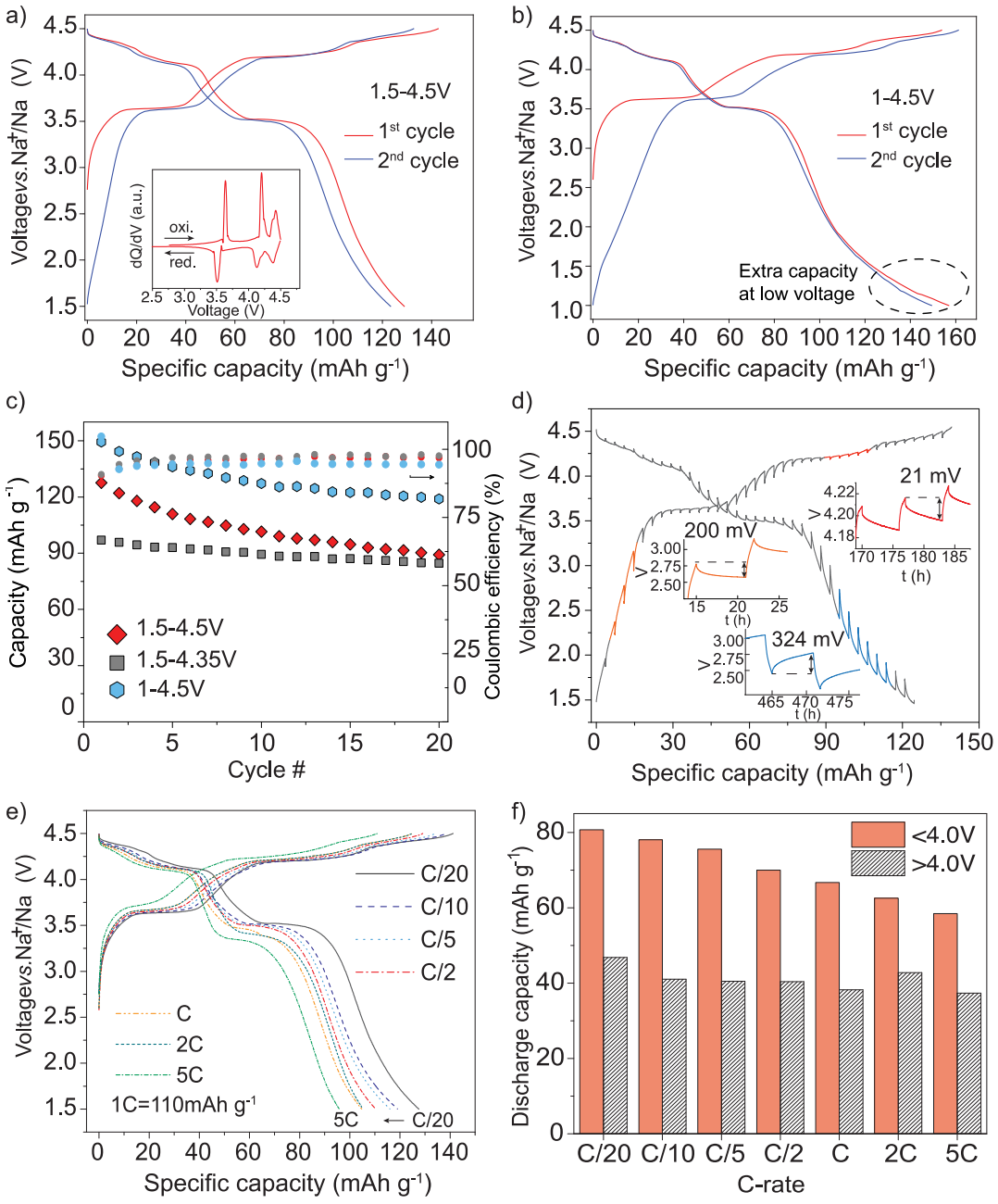


*Figure 3: Electrochemical charge and discharge of a NMCP|Na metal half-cell cycled between 1.5 and 4.5 V (a) and between 1 and 4.5 V (b) at C/20 (1C = 110*

*mAh $g^{-1}$). c) Cycling performance and coulombic efficiency of NMCP in different voltage windows. d) GITT curve of NMCP|Na metal half-cell during second cycle. Charging was performed at C/30 for 1 h, followed by a relaxation time of 6 h. Voltage vs. time plots are presented as insets to highlight the relaxation intervals. e) Rate performance of NMCP charged and discharged at C-rates ranging from C/20 to 5C between 1.5 and 4.5 V. Note that we use 1C=110 mAh $g^{-1}$ (2Na) but not the theoretical capacity 166 mAh $g^{-1}$ (3Na) to better compare with other NASICONs. f) Discharge capacity of NMCP for voltages > 4 V (red) and < 4 V (shaded) at various C-rates.*

The electrochemical performance of the NMCP|Na metal half-cell was then investigated at temperatures well above and below RT. A capacity cutoff (100 mAh $g^{-1}$, ~2Na) was applied during charge to ensure that the samples at different temperatures were deintercalated to the same Na content, and a 1.5 V voltage cutoff was applied during discharge. The charge and discharge curve at −10 °C, 20 °C and 50 °C in Figure 4a can be divided into a low-voltage region (~3.6 V) and a high-voltage region (~4.2 V). The capacity of the low-voltage region increases substantially with increasing temperature, whereas the trend for the high-voltage region is clearly reversed: from −10 °C to 20 °C and then 50 °C the charge capacity of the low-voltage region is extended, whereas the discharge capacity of high-voltage region is decreased. This observation suggests that at low temperature, during discharge, more capacity is delivered at high voltage. This finding is unusual as improved electrochemical performance is expected at high temperature because of the improved Na kinetics; however, the performance of NMCP at −10 °C is as good as that at high temperature and even better in terms of

energy density. The inset of Figure 4a clearly shows that the high-voltage discharge capacity at −10 °C is almost twice that at 50 °C. Same behavior is observed using a 4.5 V voltage cutoff (Figure S5). The cycling performance at −10 °C, 20 °C, and 50 °C is summarized in Figure 4b. NMCP exhibits negligible capacity loss with nearly 100% columbic efficiency at all the temperatures after ten cycles, indicating its stable all-temperature electrochemical performance.

Because of the poor electrical conductivity of NMCP, the electrochemical performance is greatly affected by the carbon content. Cathode films with different carbon contents were prepared and tested under identical conditions (Figure S2). As the active material:carbon:polytetrafluoroethylene (PTFE) ratio changes from 70:30:0 to 70:30:5 and then to 70:20:10, the discharge capacity first remains relatively constant from 131 to 130 mAh $g^{-1}$ and finally drops to 112 mAh $g^{-1}$, indicating that the electrical conductivity of the cathode composite is a limiting factor. Moreover, the largest discharge capacity, 131 mAh $g^{-1}$ (1.5–4.5 V) was achieved using a 70:30 active material to carbon ratio without any PTFE binder (method), which is electronically insulating, yielding a high energy density of ~470 Wh $kg^{-1}$.

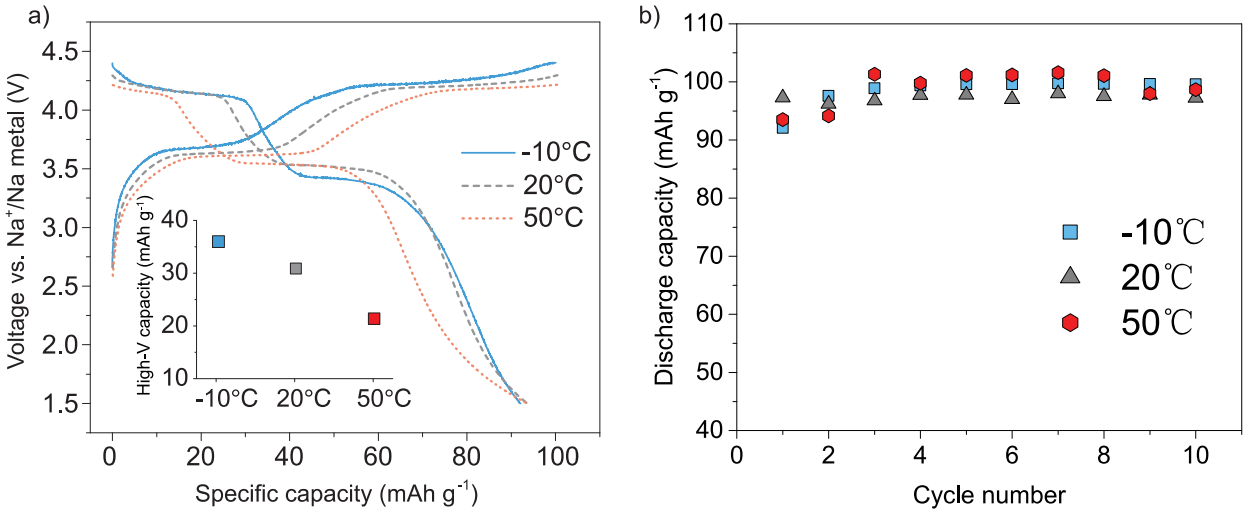


*Figure 4: a) NMCP|Na metal half-cell cycled at −10 °C, 20 °C, and 50 °C at C/10. The charge capacity is limited to 100 mAh $g^{-1}$. The inset shows the discharge capacities of the high-voltage plateau cycled at different temperatures. b) Capacity retention of NMCP during first 10 cycles at C/10. The charge capacity is limited to 100 mAh $g^{-1}$, and the voltage cutoff for discharge is 1.5 V.*

X-ray absorption spectroscopy analysis was conducted to investigate the redox mechanism of NMCP. Several *ex situ* samples were prepared at different charge and discharge states as shown in Figure S3. Figure 5a and 5b show the X-ray absorption near-edge structure (XANES) for the Mn K-edge and Cr K-edge, respectively. Both the Mn and Cr K-edge shift to higher energy during charge and return to their initial positions when discharged back to 1.5 V, indicating that both Mn and Cr are electrochemically active and reversible during cycling. Specifically, Mn and Cr redox occur in sequence: Mn is only active from the open-circuit voltage (OCV) to somewhere between 3.9 and 4.3 V, as the Mn K-edge spectra at 4.3 V and 4.5 V are almost identical. Cr is active from somewhere between 3.9 and 4.3

V to 4.5 V but not at lower voltage. While it is possible that within a small voltage region near 4.3 V, Mn and Cr redox could be both active, as the calculated voltage of $Mn^{3+/4+}$ and $Cr^{3+/4+}$ redox are extremely similar (Figure 1), it has been experimentally reported that Cr redox in NASICON framework tends to be higher than Mn redox.[20] Therefore, it is likely that the Mn redox contributes to the first two plateaus in the charge profile (Figure 3a) of NMCP, whereas the Cr redox mainly contributes to the third. The capacities of the first two plateaus are almost equal to two electrons per formula unit, so it is plausible to assume that double redox $Mn^{2+/3+}$ and $Mn^{3+/4+}$ are active. This observation also consistent with the computational predictions in Table S3, which indicate that $Mn^{2+/3+}$ and $Mn^{3+/4+}$ redox are active from Na4 to Na2 and that the $Cr^{3+/4+}$ redox is active from Na2 to Na1.

The extended X-ray absorption fine structure (EXAFS) of Mn for samples at various charge states are presented in Figure 5c, where the first peak reflects the Mn–O bond length variation. As the pristine material is charged to 3.9 V, the first peak (Mn–O bond) shifts to the left and its intensity decreases. The reduced Mn–O bond length is consistent with the oxidation of $Mn^{2+}$ to $Mn^{3+}$, and the decrease in peak intensity can be attributed to the Jahn–Teller distortion of $Mn^{3+}$ that reduces the octahedral symmetry. Upon charging from 3.9 V to 4.3 V, the Mn–O peak intensity increases again, indicating restored octahedral symmetry and $Mn^{3+}$ ion is oxidized to $Mn^{4+}$. Note that the Mn-O peak position does not show obvious change between $Mn^{3+}$ and $Mn^{4+}$, which is consistent with several previous studies.[23, 32] When

the sample is further oxidized to 4.5 V, both the intensity and position of the first peak barely change, consistent with the conclusion from the XAS data in Figure 5a that Mn is not active at higher voltage (>4.3 V). The EXAFS spectrum of the sample after one cycle does not perfectly overlap with that of the pristine sample, indicating a slight change of the Mn local structure as not all the Na extracted during charge is intercalated back when the material is discharged to 1.5 V.

Figure 5d shows the variation of the Cr pre-edge feature, providing insight into the Cr oxidation state. The spectrum taken in the pristine state remains unchanged upon charge to 3.9 V with only a single peak at ≈5590.05 eV. Upon further charge to 4.3 V, another peak at higher energy appears and continues to grow before returning to the pristine spectrum after one cycle. This prominent pre-edge peak results from the 1s–3d quadrupole transition, indicating the existence of $Cr^{4+}$.[20] As $Cr^{4+}$ with the $d^2$ electron configuration usually has a distorted octahedral symmetry, the probability of Cr-3d and O-2p orbital mixing increases, thus increasing the probability of a 1s–3d transition; this transition is forbidden when Cr is present as $Cr^{3+}$ which has a symmetric octahedral coordination.[33] In addition, the intensity of this pre-edge peak is less than 10% of the edge height, as shown in Figure 5b, thereby excluding the existence of $Cr^{6+}$, as tetrahedrally coordinated $Cr^{6+}$ increases the pre-edge peak intensity dramatically (≈80% of the edge

height). This pre-edge feature confirms that Cr is indeed oxidized to $Cr^{4+}$ during charge.

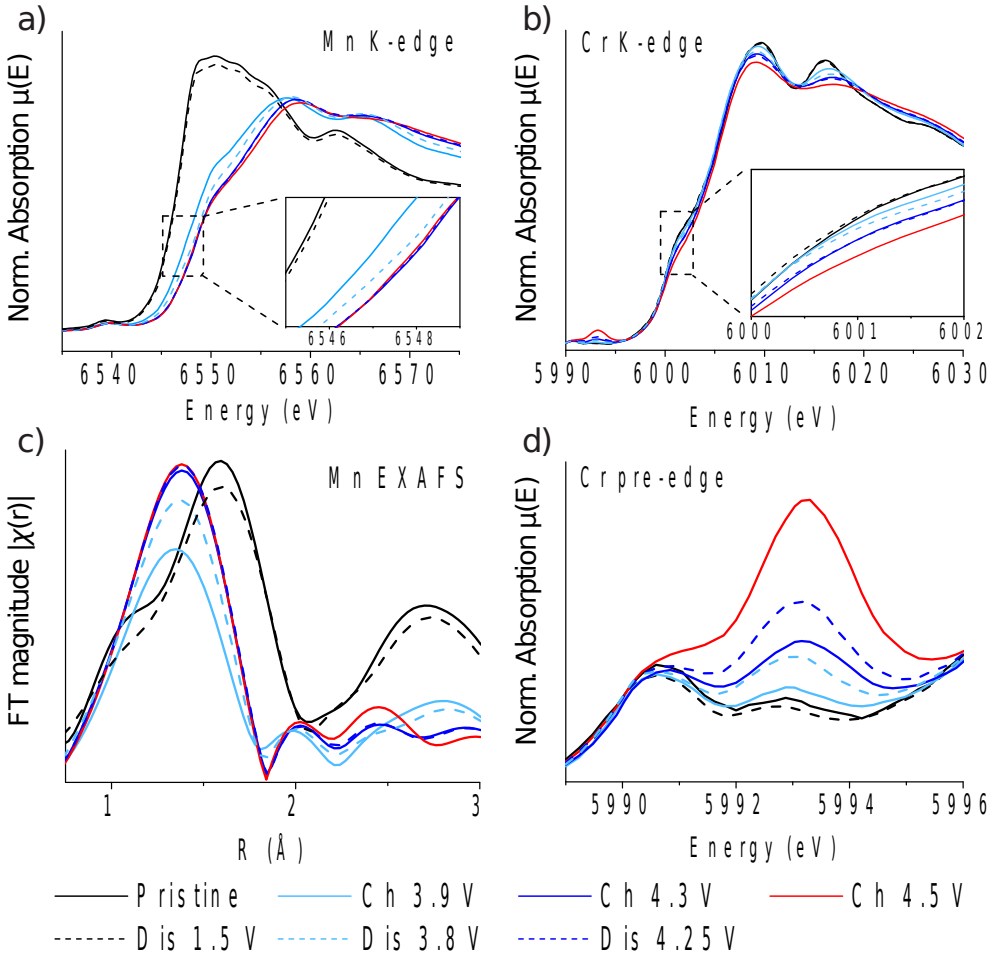


*Figure 5: XAS spectra of NMCP at different charge/discharge states: a) Mn K-edge shift and b) Cr K-edge shift. c) $k^2$-weighted Fourier transform magnitudes of Mn K-edge EXAFS spectra. d) Pre-edge feature of Cr K-edge.*

To investigate the structural evolution during charge/discharge, *in situ* XRD analysis was performed and the results are plotted in Figure 6. The four observed peaks for the uncharged sample at $x = 4$ can be assigned as the (024), (211), (116), and (300) Bragg peaks of the pristine NMCP. Between $x = 4$ and approximately $x = 3.5$, all four peaks shift slightly toward higher

angle with no additional peak evolution emerging, indicating that in this composition range NMCP forms a solid-solution. Between $x \approx 3.5$ and $x \approx 3.2$, Na is further extracted by a two-phase mechanism as evidenced by the discrete position change of the (024) and (116) peaks and the disappearance of the (211) and (300) peaks. In addition, a new peak appears at 16.2°. From $x \approx 3.2$ to the top of charge, NMCP undergoes further single-phase desodiation since the (116) and (300) peaks continuously shift to higher angle, reaching a composition of $Na_{1.27}MnCr(PO_4)_3$ at 4.5 V. The discharge of NMCP follows the same but inverse sequence: single-phase, two-phase and single-phase. This reversible structural evolution is also observed for the subsequent cycle, as confirmed by the *in situ* diffraction data of two full cycles in Figure S4.

The structural evolution of NMCP was further studied using *ex situ* synchrotron XRD. Figure 7a presents the diffraction patterns of samples at different states of charge with the extracted lattice parameters summarized in Figure 7b. The patterns for the pristine sample and sample after one cycle are almost identical, except for a slightly lower intensity for the cycled sample. In the single phase region, between $x = 4$ and $x = 3.5$, the lattice parameters $a$ (=$b$) and $c$ both decrease negligibly ($|\triangle a/a| \sim 0.17\%$, $|\triangle c/c| \sim 0.37\%$), resulting in a small overall decrease in the unit cell volume ($|\triangle V/V| = 0.7\%$). The second phase appears at 3.9 V, of which the (2-10), (113) and (300) diffraction peaks are marked by the dashed line. They continue to shift

to higher angle to the top of charge. Note that at 3.9 V, (2-10) and (104) peak are so closed to each other that they are not clearly distinguished. Upon further Na removal, (2-10) peak shifts to higher angle faster than (104) peak. As a consequence, two peaks are observed separately at 4.5 V. In this region, NMCP endures a slightly larger lattice change, with the *a* and *b* lattice parameters decreasing ($|\triangle a/a|$ = 1.18%) and the *c* lattice parameter increasing ($|\triangle c/c|$ = 1.8%). The increase in *c* lattice parameter is prominent between $x \approx 2$ and $x \approx 1$ (Figure 7b), indicating that the third Na is likely extracted from the $Na_1$ site (Figure 2b) where the absence of Na leads to large electrostatic repulsion between adjacent [$(Mn/Cr)O_6$] octahedra. The calculated lattice parameter changes are summarized in Table 1 for comparison.

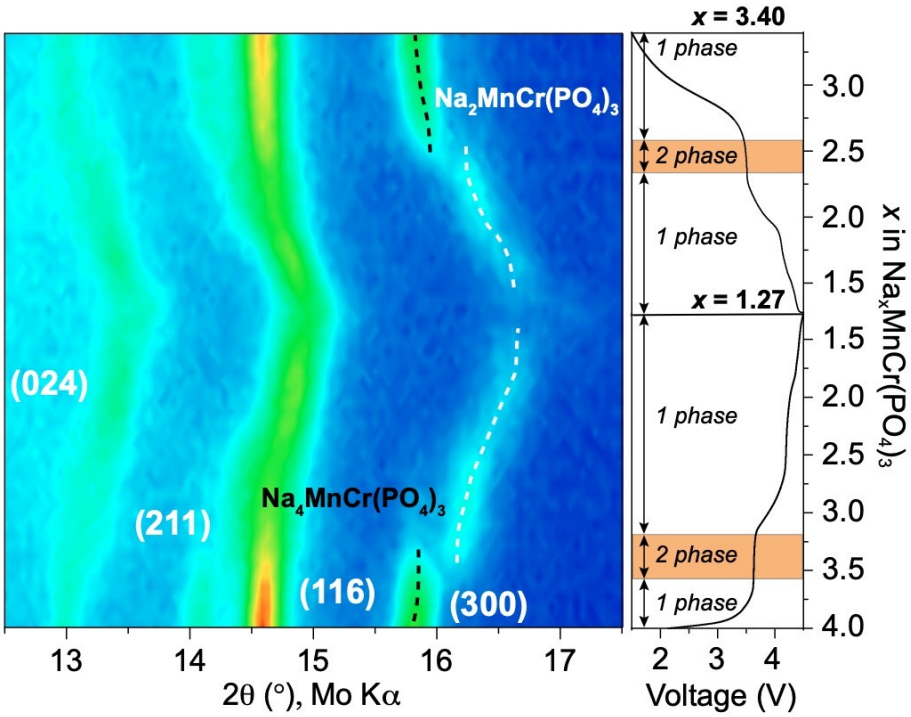

*Figure 6: In situ XRD pattern of NMCP cycled between 1.5 and 4.5 V. The current rate was C/24, and an X-ray scan was performed every hour. The corresponding voltage profile is presented on the right, where the Na content was calculated from the capacity, assuming no electrolyte decomposition contribution.*

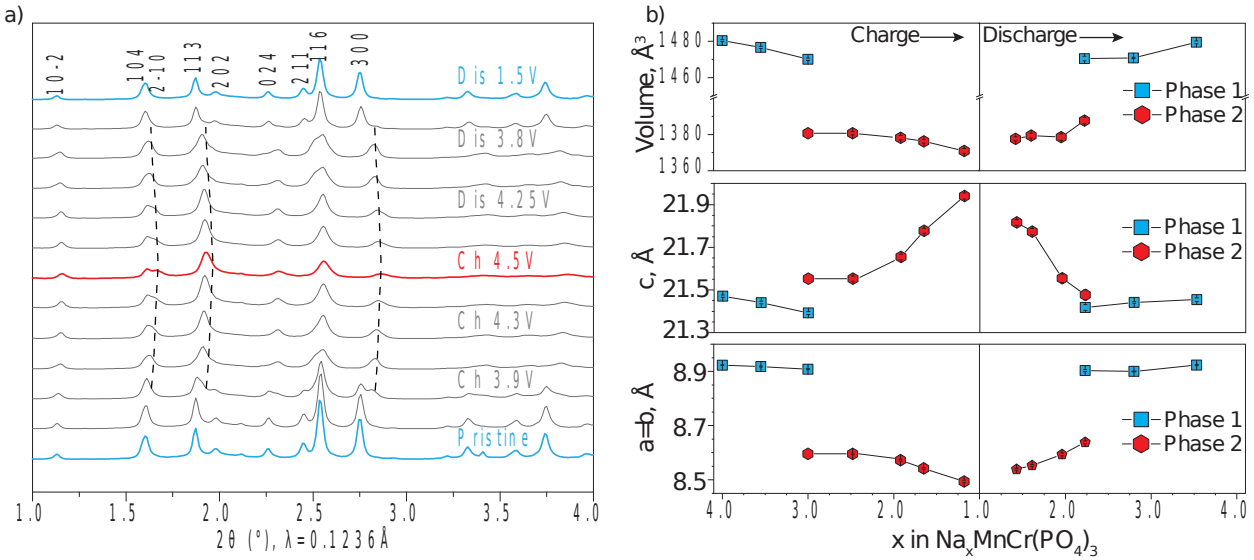


*Figure 7: a) Ex situ synchrotron XRD patterns of NMCP at various states of charge. The black dashed line denotes the appearance and disappearance of the $Na_2MnCr(PO_4)_3$ phase. The samples were prepared as shown in Figure S3. b) Corresponding lattice parameters.*

*Table 1: DFT calculated lattice parameters for $Na_xMnCr(PO_4)_3$.*

| Composition | *a*=*b* (Å) | *c* (Å) |
|---|---|---|
| Na4 | 9.08 | 21.35 |
| Na3 | 8.86 | 21.64 |
| Na2 | 8.69 | 21.80 |
| Na1 | 8.55 | 21.87 |

## Discussion

The NASICON structure is able to accommodate different transition metal cations and is synthetically accessible with various Na contents, leading to a rich chemical space and tunable electrochemical performance.[16, 18, 22, 23, 34] Among all the redox-active metals, V and Mn have been favored because they can provide double redox at high voltage ($V^{3+/5+}$ and $Mn^{2+/4+}$). However, reversible 3Na (de)intercalation has not been possible in $Na_4MnV(PO_4)_3$ because an irreversible structural change occurs after the extraction of 3Na.[25] Mn is more preferable than V from a cost and energy density perspective because the $Mn^{2+/3+}$ (3.6 V) and $Mn^{3+/4+}$ (4.2 V)[19] redox potentials are higher than those of $V^{3+/4+}$ (3.4 V) and $V^{4+/5+}$ (~4 V),[28] respectively. Hence, a Mn-based NASICON-type compound was preferred in our composition design. We show below that by systematically considering three types of Mn-based compositions, the MnCr appears naturally as the preferred compound. 1) The first compositional category contains the $Na_3Mn^{2+}M^{4+}(PO_4)_3$ compounds, which utilize $Mn^{2+/3+}$ and $Mn^{3+/4+}$ redox and possibly achieve the insertion of one more Na based on the $M^{3+/4+}$ redox; however, the reduction potential of the +4 metal is often very low (*e.g.,* NMTP, $Ti^{3+/4+}$ ~ 2.1 V), and an additional Na source such as a Na metal anode or a sacrificial salt ($NaN_3$ or $NaP_3$) is needed in practical application. 2) $Na_3Mn^{3+}M^{3+}(PO_4)_3$ compounds, which make use of $Mn^{3+/4+}$ and $M^{3+/4+}$ redox have also been considered; however, they also require an additional Na source in a full cell to use $Mn^{3+/2+}$. In addition, it is also difficult to create NASICON compounds with $Mn^{3+}$ rather than with $Mn^{2+}$

in the pristine material because of the reducing environment from the carbon source used during the synthesis of NASICONs. 3) Finally, $Na_4Mn^{2+}M^{3+}(PO_4)_3$ can be considered; this compound type can use $Mn^{2+/3+}$, $Mn^{3+/4+}$, and $M^{3+/4+}$ redox, and the pristine material contains 4Na, which is optimal for achieving electrode balance in the full cell. Therefore, a NASICON-type compound with the composition $Na_4Mn^{2+}M^{3+}(PO_4)_3$ in principle has three-electron redox at high voltage, and the trivalent metal can be $Cr^{3+}$, $Fe^{3+}$, $Co^{3+}$, or $Ni^{3+}$. The redox potentials of $Co^{3+/4+}$, and $Ni^{3+/4+}$ might be too high to access in the polyanionic framework[35] and the $Fe^{3+/4+}$ redox potential is around 3 V which is less attractive.[36] $Cr^{3+/4+}$ redox has been demonstrated to occur ≈4.5 V in NASICON-type $Na_3Cr_2(PO_4)_3$, which is within the electrolyte stability window, though significant capacity decay is observed in this compound.[20] However, in this work we demonstrate that based on the synergetic effect of Mn and Cr, $Na_4MnCr(PO_4)_3$ achieves a reasonable cyclability at a high operating voltage, and the highest energy density among all reported NASICON-type Na-ion cathodes (Figure 8).

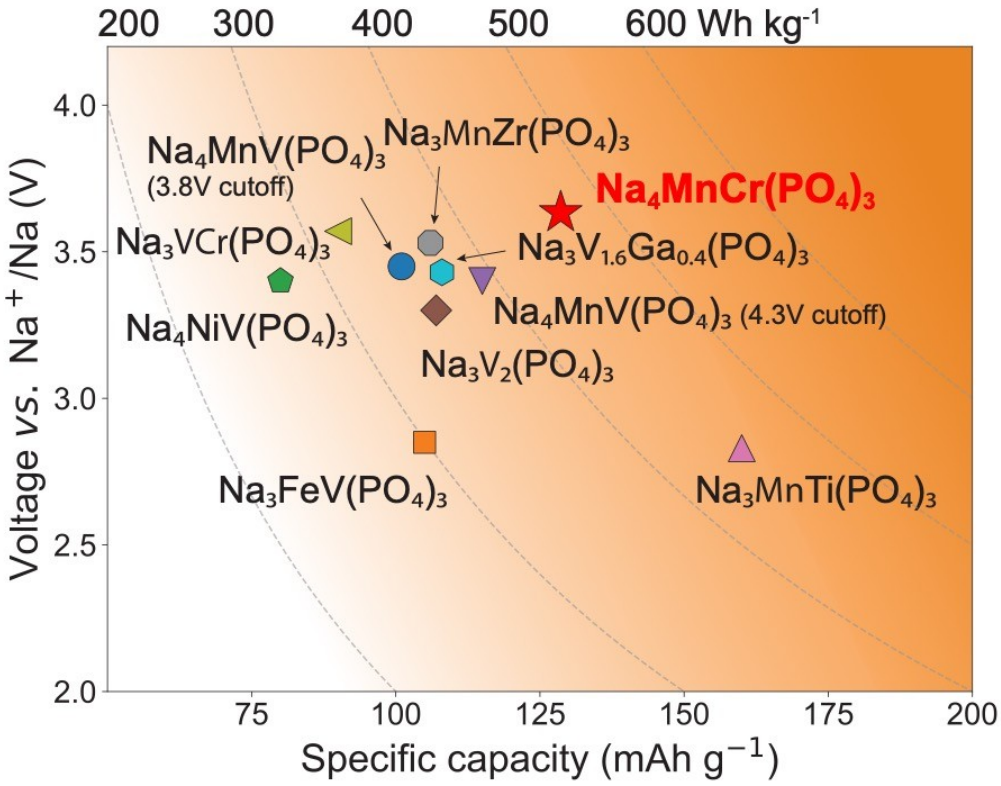


*Figure 8: Capacity vs. voltage plot of reported NASICON-type Na cathode materials.*

It is instructive to compare NMCP with another $Mn^{2+}$, $M^{3+}$ compound in this category, $Na_4MnV(PO_4)_3$ (NMVP). Although NMVP also has enough redox-active transition metal, it experiences an irreversible phase transformation when the third Na is extracted,[25] evidenced by the asymmetry behavior in the charge and discharge. A single-phase and two-phase structural transformation occur in sequence in the charge of NMVP, whereas the discharge follows a single solid-solution mechanism with no two-phase region observed. This structural irreversibility results in a low columbic efficiency of ~74%, and the subsequent charge and discharge of NMVP occurs via a single solid-solution mechanism with significant capacity fade.[25] In contrast, we

observe in the present work that NMCP has a symmetric voltage profile, *i.e.,* the charge and discharge curves both have three distinct plateaus, with the solid-solution and two-phase reaction reversibly taking place during charge and discharge. This reversible structural evolution leads to a larger discharge capacity (130 mAh $g^{-1}$) at high voltage and higher columbic efficiency (~91.5%) compared with NMVP. Our *ex situ* synchrotron XRD results also suggest that NMCP undergoes less volume change from Na2 to Na1 than NMVP (NMCP: $|\triangle a/a| = 1.18\%$, $|\triangle c/c| = 1.8\%$; NMVP: $|\triangle a/a| = 6.1\%$, $|\triangle c/c| = 2.4\%$[25]).

Because capacity fading is observed for both NMCP and NMVP after the extraction of 3Na, we computationally investigate the structural stability of the NASICON framework in the highly desodiated state by calculating the energy penalty of transition metal migration at a Na content of $x = 1$. As shown in Table S4, the calculated energy penalty associated with the migration of a $Cr^{4+}$ ($V^{5+}$) cation to the adjacent unoccupied $Na_2$ site (Figure 2b) is 2.47 eV/defect (3.01 eV/defect), which is much higher than the *M* defect formation energy in layered $Na_xMO_2$ materials which are known to suffer from structure instability at high voltage due to TM migration.[37] In addition, having Na re-occupy the TM site (TM/Na anti-site) does not necessarily reduce the energy penalty. Our calculation suggests that TM migration is unlikely in the NASICON structure even at Na content $x = 1$,

therefore the origin of capacity fading at high voltage require further investigation.

The electrochemical tests at various temperatures indicate that NMCP has a higher energy density at −10 ºC than at RT and 50 ºC if a capacity cutoff of 100 mAh $g^{-1}$ is applied. This difference is observed because the temperature affects the capacity from the low-voltage and high-voltage region differently: *i.e.*, during discharge, low temperature increases the high-voltage capacity but decreases the low-voltage capacity. Figure 9a presents the voltage profile of the first two cycles of NMCP at 50 ºC followed by a third cycle at 9 ºC. Although the high-voltage discharge region is shortened at 50 ºC, the capacity is regained during the following cycle at 9 ºC, indicating that the high-voltage capacity reduction occurring at 50 ºC is not an irreversible process. *Ex situ* XRD patterns of NMCP cycled at 50 ºC and 9 ºC are presented in Figure 9b, with no obvious difference observed at the top of charge, *i.e.,* the charged crystal structures at 50 ºC and 9 ºC are the same. This observation indicates that the different voltage profiles may result from the different Na (de)intercalation pathways at various temperatures rather than to any structural aspect at the top of charge. As revealed by the *in situ* diffraction results, the Na (de)intercalation mechanism differs at the two plateaus: for the low-voltage plateau, NMCP is desodiated via a two-phase reaction, whereas a solid-solution mechanism is observed for the high-voltage one (Figure 6) so that it should probably be referred to as a “pseudo-

plateau" consistent with the fact that the GITT relaxed voltages in this region are not constant (Figure 3d). As a two-phase reaction occurs through the nucleation and motion of an interface, extra kinetic barriers need to be overcome. High temperature will accelerate the nucleation and growth as these processes have a higher activation energy than diffusion, resulting in the elongation of the two-phase region (low-voltage region). Figure 9a clearly shows that the voltages in the low-voltage region at 50 ºC are constant (two-phase reaction), while they become not constant (solid solution) at 9 ºC. Malik *et al.*[38] reports a similar behavior of $LiFePO_4$ cathode, of which a non-equilibrium single-phase delithiation pathway is trigged by high rate to bypass the equilibrium two-phase reaction. However, in our case, direct evidence such as *in situ* XRD at various temperatures is needed to confirm this speculation. We also plot in Figure S5 the voltage profile of NMCP cycled at low temperature (9 ºC) and high temperature (50 ºC) using a voltage cutoff (1.5 - 4.5 V). Though the charge capacity at high temperature is substantially larger than that at low temperature, the discharge capacities are similar because high temperature introduces more capacity degradation at high voltage.

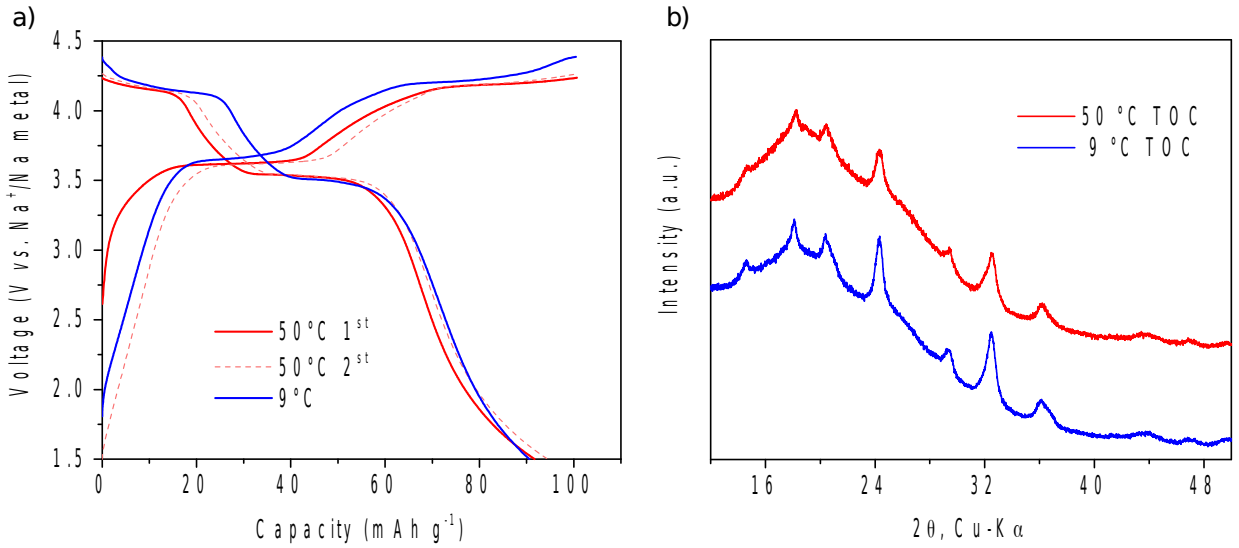


*Figure 9: a) Voltage profile of NMCP|Na metal half-cell using a 100 mAh $g^{-1}$ charge cutoff and 1.5 V discharge cutoff, at 50 ºC, C/10 for the first two cycles (Red), followed by a third cycle at 9 ºC, C/10 (Blue). b) Ex situ X-ray diffraction patterns of NMCP|$C_{sp}$|PTFE electrode cycled at 50 ºC (Red) and 9 ºC (Blue) at top of charge (100 mAh $g^{-1}$). X-ray diffraction was taken at RT immediately after cycled at different temperature.*

In conclusion, we computationally predicted the phase stability and voltage profile of a novel NASICON-type compound, $Na_4MnCr(PO_4)_3$, which is synthesized via a sol-gel-assisted solid-state method. Electrochemically, NMCP delivers a capacity of 130 mAh $g^{-1}$ when cycled between 1.5 and 4.5 V, with a high energy density of 470 Wh $kg^{-1}$. XAS analysis revealed a reversible redox mechanism based on $Mn^{2+/3+}$, $Mn^{3+/4+}$, and $Cr^{3+/4+}$ redox. Reversible and symmetric structural evolution during cycling was confirmed using *in situ* XRD and *ex situ* synchrotron XRD. The compound also has the remarkable property that it delivers higher energy density at low temperature than at high temperature.

## Methods

*First-principles calculations* were performed using DFT as implemented in the Vienna ab initio simulation package.[39] A kinetic energy cutoff of 520 eV was selected for the plane-wave basis set, and a 2 x 2 x 1 *k*-point grid was used in all the calculations. The Perdew–Burke–Ernzerhof (PBE) generalized gradient approximation (GGA) exchange-correlation functional with the rotationally invariant scheme of Hubbard-U correction[40] was applied to calculate the voltages. The values of $U_{eff}$ = 5.09 and 3.7 eV were employed for Mn and Cr, respectively, consistent with previous *ab-initio* studies of the intercalation voltage of MnZr NASICONs and Mn phosphates.[19, 41] Desodiated structures with Na/vacancy orderings were pre-screened using an electrostatic energy criterion followed by DFT geometry optimizations. Na ions were extracted in the sequence from three Na ions at the $Na_2$ sites to one Na ion at the $Na_1$ site, which is consistent with previous findings in other NASICON structures.[34, 42]

*Material Synthesis:* $Na_4MnCr(PO_4)_3$ was synthesized via a sol-gel-assisted solid-state method. First, manganese(II) acetate tetrahydrate (Aldrich, 99%) and chromium(III) nitrate nonahydrate (Sigma-Aldrich, 99%) in a 1:1 ratio were dissolved in deionized water. Then, citric acid (Sigma-Aldrich, ≥99.5%)

was added using a 3:2 (transition metal) ratio. The solution was heated at 60 °C for 2 h with magnetic stirring before stoichiometric amounts of sodium phosphate monobasic (Sigma-Aldrich, ≥99%) and sodium acetate (Sigma-Aldrich, ≥99%) were added sequentially to the solution, which was then thoroughly stirred at 90 ºC overnight to evaporate the solvent. The resulting gel-like mixture was collected, grounded, and fired at 400 ºC for 6 h in argon and then re-grounded and fired at 650 ºC for 8 h in argon.

*Structural Characterization:* High-energy X-ray powder diffraction data were collected at beamline 6-ID-D at the Advanced Photon Source, Argonne National Laboratory with a wavelength of $\lambda$=0.1236 Å. The samples were sealed in Kapton capillaries with the measurements performed using a 0.1-s exposure time for 30 s. *Ex situ* synchrotron XRD samples were prepared using a 70:30 ratio of active material:$C_{sp}$ and cycled to various states of charge at C/20 before the powder was recovered, washed, centrifuged, and collected. Lab XRD data were collected using a Rigaku MiniFlex 600 diffractometer. Data analysis was performed using Rietveld refinement[43] (as-synthesized material) and the Le Bail method[44] (*ex situ* samples) using FullProf software.[45] Structure visualization was performed with VESTA.[46]
SEM images were captured using a Zeiss Gemini Ultra-55 analytical field-emission microscope at the Molecular Foundry at Lawrence Berkeley National Laboratory.

High-angle annular dark-field scanning transmission electron microscopy and EDX mapping were performed using a FEI TitanX 60-300 at the Molecular Foundry at Lawrence Berkeley National Laboratory.

XAS data was collected at beamline 20-BM at the Advanced Photon Source, Argonne National Laboratory. Samples were prepared with a 70:30:5 active material:$C_{sp}$:PTFE ratio and cycled to various states of charge at C/20 before the powder was recovered, rinsed, and collected. All the samples were sealed with Kapton tape for XAS measurements. Data reduction, normalization, and analysis were performed using the Demeter package.[47]

*In situ* electrochemical tests were performed with a customized cell with a beryllium window allowing X-ray penetration. The experiments were conducted on a Bruker D8 diffractometer using Bragg–Brentano geometry with Mo Kα radiation. Each scan was performed for 1 h while the cell was cycled at C/24 for two full cycles.

*Electrochemical Methods:* To prepare the cathode film, the $Na_4MnCr(PO_4)_3$ powder and carbon black (Timcal, Super P) were first mixed using a Fritsch Pulverisette ball mill (with one steel sphere) for 20 min at 20 $s^{-1}$. The powder was then recovered and PTFE (Dupont, Teflon 8C) was added and mixed using a mortar and pestle before the sample was rolled into a thin film inside an argon-filled glove box. The weight ratio of active material:$C_{sp}$:PTFE was 70:30:5. To assemble a coin cell for electrochemical tests, 1 M $NaPF_6$ in a 1:1 solution of ethylene carbonate (Sigma-Aldrich, 99%, anhydrous) and diethyl

carbonate (Sigma-Aldrich, ≥99%, anhydrous) was used as the electrolyte and Na metal was used as the negative electrode. The CR2032 coin cells were assembled inside an argon-filled glove box and tested on an Arbin instrument at room temperature in galvanostatic mode.

**Acknowledgements**

This work was supported by the Samsung Advanced Institute of Technology. Work at the Molecular Foundry, LBNL was supported by the Office of Science, Office of Basic Energy Sciences of the U.S. Department of Energy under Contract No. DE-AC02-05CH11231. Use of the Advanced Photon Source at Argonne National Laboratory was supported by the U.S. Department of Energy, Office of Science, Office of Basic Energy Sciences under Contract No. DE-AC02-06CH11357. The authors acknowledge Dr. Hyunchul Kim, Dr. Guobo Zeng, and Dr. Jianping Huang for valuable discussions; Zijian Cai for assistance with the XAS measurements; and Dr. Douglas Robinson for assistance at APS.

**Bibliography:**

[1] B. L. Ellis, L. F. Nazar, Current Opinion in Solid State and Materials Science 2012, 16, 168; H. Pan, Y.-S. Hu, L. Chen, Energy & Environmental Science 2013, 6, 2338; J.-M. Tarascon, Nature chemistry 2010, 2, 510.
[2] X. Xiang, K. Zhang, J. Chen, Advanced materials 2015, 27, 5343.

[3] S. W. Kim, D. H. Seo, X. Ma, G. Ceder, K. Kang, Advanced Energy Materials 2012, 2, 710; K. Kubota, S. Komaba, Journal of The Electrochemical Society 2015, 162, A2538; D. Kundu, E. Talaie, V. Duffort, L. F. Nazar, Angewandte Chemie International Edition 2015, 54, 3431; M. D. Slater, D. Kim, E. Lee, C. S. Johnson, Advanced Functional Materials 2013, 23, 947; N. Yabuuchi, K. Kubota, M. Dahbi, S. Komaba, Chemical reviews 2014, 114, 11636.
[4] I. Hasa, S. Passerini, J. Hassoun, Journal of Materials Chemistry A 2017, 5, 4467; L. Liu, X. Li, S. H. Bo, Y. Wang, H. Chen, N. Twu, D. Wu, G. Ceder, Advanced Energy Materials 2015, 5, 1500944; N. Yabuuchi, M. Kajiyama, J. Iwatate, H. Nishikawa, S. Hitomi, R. Okuyama, R. Usui, Y. Yamada, S. Komaba, Nature materials 2012, 11, 512.
[5] M. H. Han, E. Gonzalo, G. Singh, T. Rojo, 2015, 8, 81; N. Ortiz-Vitoriano, N. E. Drewett, E. Gonzalo, T. Rojo, Energy & Environmental Science 2017, 10, 1051.
[6] C. Masquelier, L. Croguennec, Chemical Reviews 2013, 113, 6552; Q. Ni, Y. Bai, F. Wu, C. Wu, 2017, 1600275.
[7] Z. Jian, W. Han, X. Lu, H. Yang, Y. S. Hu, J. Zhou, Z. Zhou, J. Li, W. Chen, D. Chen, Advanced Energy Materials 2013, 3, 156.
[8] F. Lalère, V. Seznec, M. Courty, R. David, J. Chotard, C. Masquelier, Journal of Materials Chemistry A 2015, 3, 16198.
[9] R. Gover, A. Bryan, P. Burns, J. Barker, Solid State Ionics 2006, 177, 1495.
[10] Y. U. Park, D. H. Seo, H. Kim, J. Kim, S. Lee, B. Kim, K. Kang, Advanced Functional Materials 2014, 24, 4603; P. Serras, V. Palomares, A. Goñi, I. G. de Muro, P. Kubiak, L. Lezama, T. Rojo, Journal of Materials Chemistry 2012, 22, 22301.
[11] M. Bianchini, P. Xiao, Y. Wang, G. Ceder, Advanced Energy Materials 2017, 7, 1700514.
[12] M. Xu, P. Xiao, S. Stauffer, J. Song, G. Henkelman, J. B. Goodenough, Chemistry of Materials 2014, 26, 3089.
[13] H. Yi, M. Ling, W. Xu, X. Li, Q. Zheng, H. Zhang, Nano Energy 2018, 47, 340.
[14] S. Chen, C. Wu, L. Shen, C. Zhu, Y. Huang, K. Xi, J. Maier, Y. Yu, Advanced Materials 2017, 29, 1700431; Z. Jian, Y.-S. Hu, X. Ji, W. Chen, Advanced Materials 2017, 29, 1601925; S. Li, Y. Dong, L. Xu, X. Xu, L. He, L. Mai, 2014, 26, 3545; C. Zhu, K. Song, P. A. van Aken, J. Maier, Y. Yu, Nano Letters 2014, 14, 2175.
[15] C. Delmas, F. Cherkaoui, A. Nadiri, P. Hagenmuller, 1987, 22, 631.
[16] W. Zhou, L. Xue, X. Lü, H. Gao, Y. Li, S. Xin, G. Fu, Z. Cui, Y. Zhu, J. B. Goodenough, Nano Letters 2016, 16, 7836.
[17] Z. Jian, W. Han, X. Lu, H. Yang, Y.-S. Hu, J. Zhou, Z. Zhou, J. Li, W. Chen, D. Chen, L. Chen, Advanced Energy Materials 2013, 3, 156; Y. Yu, X. Zhang, X. Rui, D. Chen, H. T. Tan, D. Yang, S. Huang, Nanoscale 2019.
[18] Y. Jiang, J. Shi, M. Wang, L. Zeng, L. Gu, Y. Yu, ACS Applied Materials & Interfaces 2016, 8, 689.

[19] H. Gao, I. D. Seymour, S. Xin, L. Xue, G. Henkelman, J. B. Goodenough, Journal of the American Chemical Society 2018, 140, 18192.
[20] K. Kawai, W. Zhao, S.-i. Nishimura, A. Yamada, ACS Applied Energy Materials 2018, 1, 928.
[21] R. Liu, G. Xu, Q. Li, S. Zheng, G. Zheng, Z. Gong, Y. Li, E. Kruskop, R. Fu, Z. Chen, K. Amine, Y. Yang, ACS Applied Materials & Interfaces 2017, 9, 43632.
[22] Q. Hu, J.-Y. Liao, X.-D. He, S. Wang, L.-N. Xiao, X. Ding, C.-H. Chen, Journal of Materials Chemistry A 2019, 7, 4660.
[23] A. Leclaire, M.-M. Borel, A. Grandin, B. Raveau, Acta Crystallographica Section C: Crystal Structure Communications 1989, 45, 699.
[24] R. V. Panin, O. A. Drozhzhin, S. S. Fedotov, N. R. Khasanova, E. V. Antipov, Electrochimica Acta 2018, 289, 168.
[25] F. Chen, V. M. Kovrugin, R. David, O. Mentré, F. Fauth, J.-N. Chotard, C. Masquelier, Small Methods 2018, 1800218.
[26] M. V. Zakharkin, O. A. Drozhzhin, I. V. Tereshchenko, D. Chernyshov, A. M. Abakumov, E. V. Antipov, K. J. Stevenson, ACS Applied Energy Materials 2018, 1, 5842.
[27] H. Gao, Y. Li, K. Park, J. B. Goodenough, Chemistry of Materials 2016, 28, 6553.
[28] T. Zhu, P. Hu, X. Wang, Z. Liu, W. Luo, K. A. Owusu, W. Cao, C. Shi, J. Li, L. Zhou, L. Mai, Advanced Energy Materials 2019, 9, 1803436.
[29] A. Jain, S. P. Ong, G. Hautier, W. Chen, W. D. Richards, S. Dacek, S. Cholia, D. Gunter, D. Skinner, G. Ceder, Apl Materials 2013, 1, 011002.
[30] M. K. Aydinol, Journal of The Electrochemical Society 1997, 144, 3832.
[31] K. Saravanan, C. W. Mason, A. Rudola, K. H. Wong, P. Balaya, Advanced Energy Materials 2013, 3, 444.
[32] Z. Lun, B. Ouyang, D. A. Kitchaev, R. J. Clément, J. K. Papp, M. Balasubramanian, Y. Tian, T. Lei, T. Shi, B. D. McCloskey, Advanced Energy Materials 2019, 9, 1802959; L. Baggetto, K. J. Carroll, R. R. Unocic, C. A. Bridges, Y. S. Meng, G. M. Veith, ECS Transactions 2014, 58, 47.
[33] M. L. Peterson, G. E. Brown Jr, G. A. Parks, C. L. Stein, Geochimica et Cosmochimica Acta 1997, 61, 3399.
[34] O. Tillement, J. Angenault, J. C. Couturier, M. Quarton, Solid State Ionics 1991, 44, 299.
[35] R. K. Petla, R. Amin, I. Belharouak, M. T. Sougrati, H. B. Yahia, R. Essehli, "Electrochemical Investigations of High Voltage Na4Ni3 (PO4) 2P2O7 Cathode for Sodium Ion Batteries", presented at *Meeting Abstracts*, 2019; M. Nose, K. Nobuhara, S. Shiotani, H. Nakayama, S. Nakanishi, H. Iba, RSC Advances 2014, 4, 9044; P. R. Kumar, H. B. Yahia, I. Belharouak, M. T. Sougrati, S. Passerini, R. Amin, R. Essehli, Journal of Solid State Electrochemistry 2020, 24, 17.
[36] R. Rajagopalan, B. Chen, Z. Zhang, X. L. Wu, Y. Du, Y. Huang, B. Li, Y. Zong, J. Wang, G. H. Nam, Advanced Materials 2017, 29, 1605694; H. Kim, I. Park, S. Lee, H. Kim, K.-Y. Park, Y.-U. Park, H. Kim, J. Kim, H.-D. Lim, W.-S. Yoon, K. Kang, Chemistry of Materials 2013, 25, 3614.

[37] X. Li, Y. Wang, D. Wu, L. Liu, S.-H. Bo, G. Ceder, Chemistry of Materials 2016, 28, 6575; S. Kim, X. Ma, S. P. Ong, G. Ceder, Physical Chemistry Chemical Physics 2012, 14, 15571.
[38] R. Malik, F. Zhou, G. Ceder, Nature materials 2011, 10, 587.
[39] G. Kresse, J. Furthmüller, Physical Review B 1996, 54, 11169.
[40] S. L. Dudarev, G. A. Botton, S. Y. Savrasov, C. J. Humphreys, A. P. Sutton, Physical Review B 1998, 57, 1505.
[41] F. Zhou, M. Cococcioni, C. A. Marianetti, D. Morgan, G. Ceder, Physical Review B 2004, 70, 235121.
[42] S. Y. Lim, H. Kim, R. A. Shakoor, Y. Jung, J. W. Choi, Journal of The Electrochemical Society 2012, 159, A1393.
[43] H. Rietveld, Journal of applied Crystallography 1969, 2, 65.
[44] A. Altomare, M. C. Burla, M. Camalli, G. L. Cascarano, C. Giacovazzo, A. Guagliardi, A. G. Moliterni, G. Polidori, R. Spagna, Journal of Applied Crystallography 1999, 32, 115.
[45] J. Rodriguez-Carvajal, "FULLPROF: a program for Rietveld refinement and pattern matching analysis", presented at *satellite meeting on powder diffraction of the XV congress of the IUCr*, 1990.
[46] K. Momma, F. Izumi, Journal of applied crystallography 2011, 44, 1272.
[47] B. Ravel, M. Newville, Journal of synchrotron radiation 2005, 12, 537.
J. Rodriguez-Carvajal, Phys. B 1993, 192, 55.